Transfer of Epitaxial SrTiO 3 Nanothick Layers Using Water-Soluble Sacrificial Perovskite Oxides

Yoan Bourlier, Bruno Berini, Mathieu Frégnaux, Arnaud Fouchet, Damien Aureau, Yves Dumont

Transfer of Epitaxial $SrTiO_3$ Nanothick Layers Using Water-Soluble Sacrificial Perovskite Oxide

Yoan Bourlier[*,1,2], *Bruno Bérini*[1], *Mathieu Frégnaux*[2], *Arnaud Fouchet*[3], *Damien Aureau*[2], *and Yves Dumont*[1]

[1] Groupe d'Etude de la Matière Condensée (GEMaC), Université de Versailles Saint-Quentin en Yvelines, Université Paris-Saclay CNRS, 45 avenue des Etats-Unis, 78035, Versailles, France

[2] Institut Lavoisier de Versailles (ILV), Université de Versailles Saint-Quentin en Yvelines, Université Paris-Saclay CNRS, 45 avenue des Etats-Unis, 78035, Versailles, France

[3] NORMANDIE UNIV, ENSICAEN, UNICAEN, CNRS, CRISMAT, 14000 CAEN, France

KEYWORDS: $SrVO_3$, $SrTiO_3$ pseudo-substrate, sacrificial layer, silicon, water soluble

ABSTRACT

Integration of functional thin film materials with adapted properties is essential for the development of new paradigms in information technology. Among them, complex oxides with perovskite structures have huge potential based on the particularly large diversity of physical properties. Here we demonstrate the possibility of transferring perovskite oxide materials like $SrTiO_3$ onto silicon substrate using an environmentally friendly process at nanoscale, by means of a water-soluble perovskite sacrificial layer: $SrVO_3$. Based on *in situ* monitoring atomic force microscopy and photoemission studies, we reveal that dissolution is initiated from a strontium rich phase at the extreme surface of $SrVO_3$. The transferred nanothick $SrTiO_3$ layer on silicon presents an effective morphology and monocrystalline quality, providing a proof of concept for the integration and development of an all perovskite oxide electronics or "oxitronics" onto any Si-based substrates.

GRAPHICAL ABSTRACT

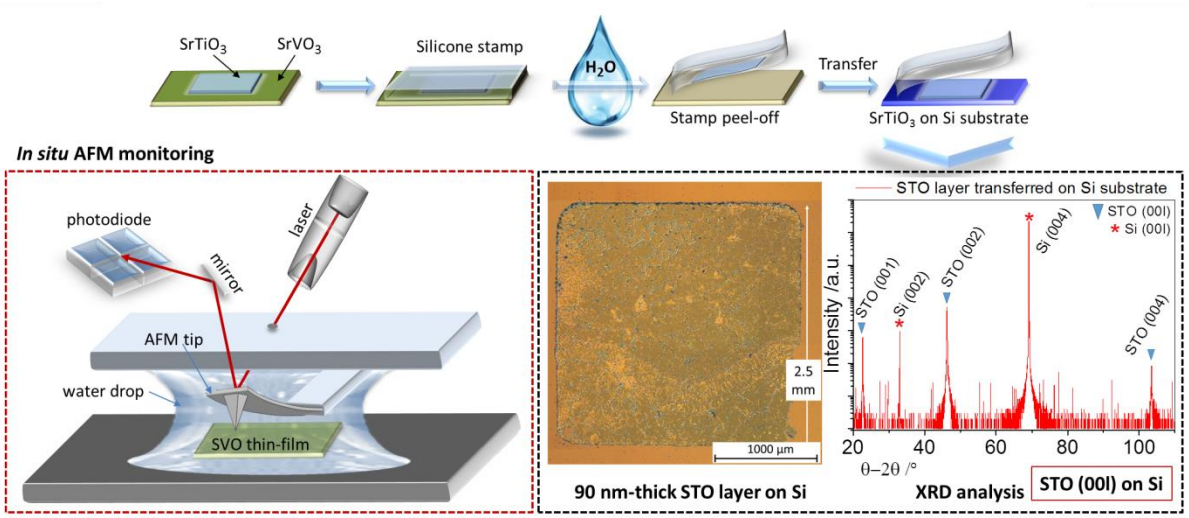

MANUSCRIPT

INTRODUCTION

Thin films technology, particularly from ABO_3 perovskite oxides, has always been considered as strong impactful research for science and technology in a perspective beyond silicon electronics.[1-3] Tremendous optical and electrical responses can now be induced at nanoscale, where significant results have been demonstrated, for example the presently famous and extensively studied $LaAlO_3/SrTiO_3$ heterostructure.[4-12] However, the growth of functional perovskite oxides on silicon or amorphous substrate like glass remains a long-standing challenge due to mechanical and chemical incompatibilities between the supports and the crystalline structure of the film. Indeed, a SiO_2 layer at the surface avoids a direct epitaxy and the perovskite oxide films can be grown only at the cost of high temperature (in order to crystallize) and only in polycrystalline form, which generally decreases the intensity of the targeted functional properties. This is due to the inherent anisotropies in pristine or distorted perovskite oxide structures. Different approaches have been developed recently to break through this critical technological barrier. First, special care can be used to remove this SiO_2 protective layer and stabilize the Si surface. This approach has been developed by Mc Kee et al.[13] in order to stabilize a buffer layer of $SrTiO_3$ (STO). Furthermore, significant efforts have been made to develop STO buffer layer on silicon using molecular beam epitaxy (MBE)[14-21] or other associated techniques such as hybrid MBE (hMBE) giving the latest great improvements.[22] However, these buffer layers are deposited at high temperature, and are barely scalable at industry level. Furthermore, this STO/Si interface remains compressively strained with defects at interface.[23] Recent promising work shows the possibility of growing STO on Si using only

pulsed laser deposition (PLD), but the resulting films are oxygen-deficient due to the use of a low oxygen pressure to preserve an intimate interface.[24]

An alternative for the growth of perovskites on amorphous substrate is the use of nanosheets acting as seed layers. These nanosheets are deposited onto the substrates by Langmuir-like deposition using soft chemistry and the most common one is $Ca_2Nb_3O_{10}^-$.[25-33] These nanosheets are 2D materials, with a thickness of 1 to 2 nm and in-plane length from 500 nm to a few micrometers. The in-plane lattice parameter is 0.386 nm, close to the targeted perovskite used. These nanosheets are nevertheless randomly deposited on the substrate. Consequently, the final film is textured out of plane and presents in most of the cases a random orientation in plane. Another similar work using 2D materials was reported of the growth of STO using PLD on graphene coated Si substrate; but even when a high (00l)-oriented crystalline STO is reported, other crystalline orientations are also observed.[34]

Another approach is the use of a sacrificial layer (SL) which preserves the in plane orientation and retains the structural quality of the transferred film. This process implies the deposition of the targeted functional monocrystalline film on a SL which can be dissolved by chemical treatment depending on its nature. The resulting freestanding functional monocrystalline film is then released onto another substrate. This process was first initiated to transfer metallic layers with NaCl crystals acting as SL and dissolving in water.[35] After several years, the process evolved to transfer much more complicated materials such as graphene layers, using hBN flakes,[36,37] or by dissolving Cu or Ni foils in $FeCl_3$ and HCl chemical baths.[38-43] Transfer of perovskite oxide crystalline layers such as $PbZr_{0.2}Ti_{0.8}O_3$ (PZT) or $SrRuO_3$ (SRO) using SL was investigated later, using either $La_{0.7}Sr_{0.3}MnO_3$,[44] or directly STO substrate, [45] as SL with their dissolution in HCl or HF respectively. Nevertheless, the transferred film must be

strongly chemically stable to those acids, which limits the choice of the materials to be transferred. Alternatively, another phase of $Sr_3Al_2O_6$, is water soluble and can also be used as SL.[46,47] Even if this material is interesting, special care has to be considered for the growth of the transferable heterostructure, because of the possible change of crystal structure rendering $Sr_3Al_2O_6$ insoluble.[48]

Ideal SL materials for functional perovskite oxides should be of the same family of materials, with a close lattice parameter, and present water solubility. In the present study, we demonstrate that strontium vanadate perovskite oxide: $SrVO_3$, noted SVO, is a good candidate for perovskite SL as it fulfilled all these conditions. Bulk $SrVO_3$ presents a cubic crystal structure with lattice parameter of 0.384 nm,[49] and is well adapted for the growth of all perovskites. Recent research on SVO has shown that this material is a promising transparent conductive oxide for integration of new devices in microelectronics industry.[50-52] Furthermore the surface of this material can be adjusted under specific growth conditions in order to obtain either a very smooth surface with a global roughness (in root mean square or RMS) of 0.5 ± 0.1 nm or a surface governed by auto-organized nanostructures. These nanostructures have already been identified as crystallites of Sr-rich phases of $Sr_3V_2O_8$.[53,54] In our previous study, a selective etching of these Sr-rich nanostructures was evidenced using water. Moreover all Sr-rich phases were found to be removed from the surface by the action of water.[55]

In this paper, we expose the process of SVO dissolution in water, proving that SVO can be used as a SL for perovskite oxides transfer. Through AFM and XPS analyses, we show that strontium rich phases exist at the surface of SVO layers. Such phases are obtained at the end of the growth, as already seen from STO surfaces where SrO surface segregation takes place after annealing,[56-58] and are essential to initiate the SVO solubilization by preferential etching. At

first, two different surfaces, a smooth one and another presenting the Sr-rich nanostructures, were considered. Finally, we are showing the transfer of STO thin films. This latter compound is widely used as a substrate for epitaxial growth of a wide range of perovskite oxides with numerous different functionalities. Transferring well-conformed thin films of STO onto Si is a first step towards the intriguing challenge to make efficient epitaxial regrowth and developing Si-integrated technologies with based-oxide electronic devices for a new dawn of "oxitronics".

RESULTS

A. In situ monitoring of the $SrVO_3$ layer dissolution in water

Study of the SVO layer dissolution in water can be observed in **figure 1** for two types of surface morphology: the smooth one and the nanostructured one. First, a dynamic imaging concerning a 40 nm-thick film with nanostructured surface is investigated by *in situ* atomic force probe (AFM) monitoring, in liquid mode (see the layout in **figure 1a**). From the numerous AFM micrographs taken in liquid mode analysis, an editing video on the *in situ* dissolution of the nanostructured SVO thin film through the action of water was produced and is available as supplementary information (SI) **S1** (see the attached MPEG file to the web version of this article) with an associated graph of roughness evolution (root mean square or RMS) through acquisition time.

Then, three AFM images collected from the video are shown in **figure 1b**, one before water contact, one after 7 min, and one after 2 h 04 min. We observe a relatively fast dissolution of the nanostructures in the first minutes in water. These nanostructures were already analyzed by transmission electron microscopy (TEM) as $Sr_3V_2O_8$ phase,[53] and also described as half-buried

through the surface,[54,55] where the dissolution in water first leaves their imprints on the surface. Thus, a preferential etching of these Sr-rich nanostructures is evidenced using water. Then, for longer times in water (from 3 min to 52 min), the roughness progressively increases and SVO layer dissolution is initiated around the nanostructures imprints. After more than 50 min, the nanoimprints are no longer discernable, SVO layer dissolution increases and the entire film starts to decompose in larger aggregates until it almost totally disappears after 2 hours.

In comparison to the SVO nanostructured thin film, the dissolution of the SVO smooth thin film is presented in **figure 1c**. This film is 40 nm-thick and presents a low roughness of 0.6 nm (root mean square or RMS), characterized by AFM. In this experiment, the middle of the smooth SVO layer is covered by a protective polymer resin, leaving unprotected both sides of the sample. After one day in water at room temperature and without stirring, the SVO uncovered zones are completely dissolved, with respect to film center which remains intact. The protective polymer resin can be removed in acetone in order to access the pristine SVO layer. Indeed, SVO smooth thin films are water soluble. Since these thin films are proven to be Sr-rich on their surfaces,[55] we can affirm that the dissolution of SVO is initiated by them. Furthermore, SVO thin films containing nanostructures appear readily soluble compared to the smooth thin films where dissolution takes longer. Thus, the kinetics of the SVO thin film dissolution seems to be accelerated by the effective roughness resulting from the imprint of the nanostructures.

B. Study of $SrVO_3$ and $SrTiO_3$ nanothick layers during transfer

In the light of these observations, we have shown that SVO layer can be used as a water-soluble SL for transferring a thin film of perovskite oxide such as STO onto silicon (Si) substrate. **Figure 2a** presents the outline of the transfer process, similar to other works.[42,46] First, a 20 nm-thick SVO film was grown onto a STO substrate, followed by a 90 nm-thick STO

film, using pulsed laser deposition (PLD) technique. The STO thin film was deposited through a mechanical mask,[59] leaving a smaller area of the STO film (2.5×2.5 mm²) compared to the SVO film deposited on the entire STO substrate (10×10 mm²). This difference in size will ease the future transfer of the STO layer.

Within the transfer process, the surface of the sample is first covered with a silicone type film serving as a stamp (see step 1 in **figure 2a**). The success for transferring the totality of the STO layer relies on the use of commercial "screen protector" (SP) film. Such SP film are basically constituted of a silicone coating on back side (applying in front of the STO thin film, and of a poly-ethylene-terephtalate (PET) film on its front side for the rigidity of the whole film. The use of SP film has been particularly chosen compared to other silicon type resin film such as (poly-dimethyl siloxane) PDMS film. Indeed, when PDMS film was used, we encountered difficulties for transferring the entire STO layer. Supporting information **S2** shows a STO layer initially of 3.9×3.9 mm² square-sized onto Si substrate where less than 20 % of the area is finally transferred by the use of PDMS film as intermediate support. According to the work of X.-D. Chen *et al.*[42] about transfer of graphene films, the transfer efficiency and integrity is strongly dependent o, the surface tension of each layer. Contrary to SP film which has the ability to easily transfer the supported film, transfer using PDMS film is very sensitive to pressure and release time.[60] This can be explained by a smaller work of adhesion at the SP/STO layer interface than the PDMS/STO layer interface.

Figure 2b illustrates the XPS mapping analysis on the corner of the square-shaped STO/SVO stack before transfer. STO area is highlighted by the presence of Ti2p (at 459.0 eV) and the Sr3d (at 134.0 eV) signals. Corresponding high-resolution energy spectra for associated Ti2p and Sr3d spectral windows are generated from the "STO area" zone (see **S3** in SI). XPS

chemical composition of the STO surface gives a cationic ratio "Sr/Ti" of 1.03 ± 0.05. The "SVO area" is also clearly delimited by the V2p (at 517.1 eV) and the Sr3d (at 132.4 eV) spectral regions. The generated spectra of Sr3d in the "STO area" and "SVO area" are definitely distinct. The different binding energies indicate two different chemical environments. The XPS chemical composition of the "SVO area" reveals a cationic ratio "Sr/V" of 1.44 ± 0.05. This Sr-rich ratio from the SVO layer is in good agreement with a previous study evidencing that Sr-rich phases exist at the extreme surface of these SVO thin films.[55] As Sr-rich phases were found to be readily soluble in water, this will be an asset for its use as a SL. **Figure 2c** represents AFM analyses of the STO and SVO surfaces. We first observe a very smooth and homogeneous STO surface with a very low RMS of 0.56 nm. However, SVO is characterized by the presence of nanostructures identified as $Sr_3V_2O_8$ crystalline structure as previously discussed.[53] This fact is due to the reaction between the masked part of SVO and O_2 partial pressure during the growth of STO layer. The presence of nanostructures in the SVO area reinforces the fact that the surface is composed of Sr-rich phases.

After applying the SP film at the surface of the STO layer, the sample is immersed in water at 50°C during about 5 days, under stirring, until all the SVO underneath layer is completely dissolved. The relatively long time of dissolution of the SVO SL can be explained by the efficient sealing of the surface with SP film. However, the process can be accelerated by adding a surfactant to lower the surface tension of water. Furthermore, we observed that a slightly alkaline aqueous media at pH near 8 (by adding KOH salt for instance) help to reduce the dissolution time of the SL. When the entire SVO layer is dissolved, the sample is carefully released from the water and SP is removed by slowly peeling off the film from the substrate (step 2 in **figure 2a**). At this step, as observed in **figure 3a**, STO thin film is released from the initial

substrate to the SP film. Thus, we can analyze the back-side of the STO layer on SP film, which was in contact with SVO. **Figure 3b** shows the XPS survey spectrum of the STO thin film standing on the SP stamp. It indicates the presence of the chemical elements Si, Sr, C, Ti and O by their main spectral signatures of Si2p, Sr3d, C1s, Ti2p, and O1s, at their respective binding energies of 101 eV, 132 eV, 284 eV, 460 eV, and 532 eV. In addition to the peaks associated with the STO, silicon is detected. As we can see in **figure 3a**, the free standing STO film is partially cracked. Therefore, XPS analysis also detects the SP film related to the Si spectral signature. **Figure 3c** shows the XPS high resolution energy spectrum of the O1s-V2p region of interest. The O1s is clearly divided in two different components, one at a binding energy of 531.5 eV, "O1s (Si-O),(C-O)" attributed to SP film spectral signature and organic contamination, and one at a binding energy of 528.5 eV, "O1s (M-O)" attributed to the STO transferred layer. However, no V2p signature was found on this spectrum, which means that no vanadium was detected or its amount is below the XPS sensitivity threshold (0.1 at.%). Therefore, the SVO layer is fully dissolved by our process. Furthermore, the STO layer standing on SP is analyzed by XRD analysis (**figure 3d**). A preferential orientation of STO perpendicular to the [001] direction is observed with STO (001) and STO (002) Bragg peaks at 2θ angles of 22.68°, and 46.18°, respectively. The broad peak at 25.88° is related to SP template (amorphous SiO_2 lattice). These analyses confirm that the entire SVO layer is dissolved, leaving a free-standing crystalline STO film with the pristine orientation.

C. Description of the final $SrTiO_3$ nanothick layer transferred onto Si substrate

The final step is then to transfer the STO standing on the SP film onto Si substrate by making a physical contact (step 3 in **figure 2a**). An annealing at 70°C for 10 min is also performed to dry the layer before gently peeling off the SP film. In **figure 4a**, an optical image of

the STO layer on Si is shown. We observe that the entire STO layer is transferred on Si substrate. Even if some cracks remained, the STO transferred layer is a well-define 2.5×2.5 mm² square-shaped characterized by domains larger than 200 µm. To further improve the quality of the perovskite transferred layer, two main optimizations can be considered. STO upper layer could be protected before conducted the SL process, using for example a photosensitive resin in order to lower the stress during transfer. We can also transfer a perovskite oxide layer with a bulk lattice parameter closer to the one of SVO (a = 0.3840 nm in theoretical values), such as $LaAlO_3$ (a = 0.3790 nm) compared to STO (a = 0.3905 nm) to reduce strain at interface.

Figure 4c represents the XPS mapping of the STO transferred layer onto Si substrate. The chemical cartography of the transferred layer is revealed by the presence of the main spectral signatures of Ti2p (458.0 eV), Sr3d (133.5 eV), and O1s (529.0 eV) inside the "square" of STO, shaped by the spectral signature of Si2p (99.0 eV). It proves that strontium and titanium are effectively transferred inside this area. These chemical maps are used to generate an averaged spectrum of each spectral region of interest where the associated spectra are visible in supplementary material (**S4** in SI). The resulting XPS chemical composition is characterized by a cationic ratio "Sr/Ti" of 0.96 ± 0.05 which is relevant compared to the analyzed "STO area" from the sample before processing the transfer (**figure 2b**). The O1s spectra is fitted with the previously introduced approach assuming two different O1s chemical environments: "O1s (Si-O),(C-O)" and "O1s (M-O)". Due to XPS mapping information, the oxygen stoichiometry of the STO layer can be also evaluated. "(Sr+Ti)/O" oxygen ratio is then extracted, through quantification of Sr3d, Ti2p and O1s (M-O) contributions, and was estimated to "0.71± 0.05" which is slightly higher than a STO oxygen stoichiometry of 0.67 for the theoretical "(Sr+Ti)/O"

ratio. This definitely evidences the conservation of the STO layer chemical composition after transfer onto Si.

In addition, **figure 5a** shows a 2x2 μm² AFM image of the STO transferred layers, selected from an area free of cracks. A well-preserved smooth and homogeneous surface is observed, characterized by a low roughness of RMS = 0.66 nm, similarly to the one measured on STO surface before transfer (RMS = 0.56 nm, see **figure 2c**). The conservation of the surface roughness proves the good quality of the transferred layer. The AFM height scan analysis in **figure 5b** is taken at the side of the reported STO layer. It reveals an averaged thickness of 88 nm, which is in good agreement with the original thickness of STO layer (90 nm-thick STO layer assumed by the PLD process). It confirms that only SVO was dissolved and that the entire STO thickness is transferred.

Most importantly, XRD analysis of the STO layer on Si substrate is performed (**figure 5c**). The Bragg peaks at 2θ angles of 32.99°, and 69.13° are associated to (002) and (004) planes of the Si substrate. STO Bragg peaks corresponding to (001), (002), and (004) indexes, are visible at 2θ angles of 22.66°, 46.25°, and 103.48°, respectively. It proves that the STO transferred layer is well crystallized with its original preferential orientation preserved, following the (00l) crystalline planes. Moreover, the Laue oscillations around STO (002) peak is measured and simulated (represented in **figure 5d**), giving a lattice parameter of c = 0.392 nm and a number of 230 unit-cells. The resulting thickness estimation of 90 nm is in perfect agreement with the ones calculated from AFM height scan and estimated from PLD process conditions. The same observation was done on thinner STO layer using a 20 nm-thick square of 3.9×3.9 mm² (see **S5**, **S6**, and **S7** in SI, for microscopy images, AFM analyses, and XRD analyses respectively). These well-resolved Laue oscillations up to high order confirm the atomic flatness of the STO in the

rear face and the good quality of an intimate STO/Si interface. All these measurements demonstrate that the initial crystalline structure, thickness, and roughness on both sides of the STO thin film are conserved upon transfer onto Si substrate.

Such featured results conclusively show that SVO layer can be used as a SL to report STO thin film onto Si substrate, encouraging a future vertical integration onto Si substrate of other perovskite oxides and/or associated heterostructures.

CONCLUSION

In this paper, we demonstrate the feasibility of transferring $SrTiO_3$ (STO) perovskite oxide thin films onto Si using $SrVO_3$ (SVO) as sacrificial layer (SL). The presented process is soft, low-cost, and environmentally friendly with only water as solvent. The process of SVO dissolution was studied by *in situ* AFM monitoring. We show that existence of Sr-rich phases at the extreme surface of SVO thin film is a clue to initiate its dissolution in water. The STO transferred layer onto Si exhibits a similar roughness and thickness than the ones before transfer, and most importantly, the initial stoichiometry and monocrystalline structure following the (00l) oriented plans are preserved. Transferring homogeneous and well-conform STO oxide layers using a SL of perovskite $SrVO_3$ is opening a new way for perovskite oxides integration onto Si substrate and other supports such as glass or flexible substrates. This proof of concept remains the crucial step for direct integration of such oxides in microelectronic and the development of a new electronics based on functional perovskite oxides.

Experimental Section

Epitaxial thin films growth conditions: $SrVO_3$ (SVO) and $SrTiO_3$ (STO) targets for pulsed laser deposition were prepared in the laboratory from high purity binary oxides powders (SrO/V_2O_5 and SrO/TiO_2) by standard ceramic processing method. The pressed pellet was sintered in air with additional oxygen flow. The "Sr/V = 1" and "Sr/Ti = 1" target metallic ratios were controlled by chemical titration. Depositions of both layers were performed in an ultra-high vacuum chamber with base pressure of 5×10^{-7} Pa. Targets were ablated using a KrF laser with a wavelength of 248 nm and 20 ns of pulse duration. Single crystal (SurfaceNet GmbH) STO (100) substrates ($10\times10\times0.5$ mm^3) were used. The laser fluency was about 1.85 J/cm^{-3} for SVO and STO. The distance between target and substrate was kept to 5 cm. The temperature and oxygen pressure for $SrVO_3$ layer was maintained to 760°C and 1.2×10^{-4} Pa, respectively.[53] In this conditions, SVO film show an excellent conductivity with a R300/R2=2.4 at the state of the art for PLD growth onto STO (100).[61] The thickness was estimated to 20 nm from RHEED measurements. Then, a shadow mask was pressed to create four STO square per sample of 2.5×2.5 mm² each. A shadow mask of 3.9×3.9 mm² was also used to create larger square-shaped areas. Temperature was rapidly decreased to 720 °C (approximately 4 min) and pressure was kept constant during the beginning of STO growth to minimize the appearance of nanostructures on the underlying layer and progressively increased to 7.5×10^{-6} Pa in order to obtain a better oxygenation. 90 nm-thick layer of STO was deposited. Samples were cooled directly after the growth with the same pressure in 2 hours. A 20 nm-thick layer of STO was also deposited in the same growth conditions with exception that the shadow mask was applied for both SVO and STO layers. A longer time to dissolve the entire SVO layer was observed probably due to the

absence of the step between the two layers. The corresponding STO layer transferred onto Si substrate is shown in supporting information (relative to **figures S5, S6** and **S7**).

Thin films transfer method: All $SrTiO_3$ (STO) layers were transferred using commercial "screen protector" (SP) sheets (PET/silicone film). SP film was adhered to STO surface sample and introduced into water at a temperature of 50°C with stirring for 5 days, in order to dissolve the entire SVO layer. After the complete etching of SVO, the SP film supporting the STO layer was applied onto Si substrate. The SP film was then released after a short annealing at 70°C for 30 min to dry the film. A single STO/SVO thin film sample was partially transferred onto Si substrate by using a poly-dimethyl siloxane (PDMS) resin film (see **figure S3** in supporting information). The synthesis of PDMS film was conducted using a Dow Corning® 184 Silicone Elastomer.

Surface characterizations details: A Dimension ICON (Bruker) Atomic Force Microscope was employed in PeakForce Tapping mode to control the morphology of both SVO and STO thin films (see **figure 2c** and **figure 5a**) using commercial silicon tips on a nitride lever with 70 kHz resonant frequency and 0.4 $N.m^{-1}$ spring constant (ScanAsyst-AIR Bruker). The scanning speed was kept constant at 2 $\mu m.sec^{-1}$ in order to compare RMS for images of different size. More specifically, a sharpened ScanAsyst-Fluid$^+$ tip (Bruker) was used in a fluid cell mounted on a 90 μm × 90 μm × 14 μm scanner to follow by *in situ* monitoring the dissolution of the SVO layer in deionized water as function of time (see **figures 1a** and **b**). In order to pursue this *in situ* AFM analysis, an image was first acquired in air to obtain the initial state. Then, a water droplet was placed on the tip by using a syringe, and another droplet deposited on the sample, giving the time t = 0 of the experiment. The scanner is lowered until the droplet on the cantilever joins and formed a meniscus with the droplet on the sample (see **figure 1a**). Consequently, the scan area is

not exactly the same than the first image in air. For faster acquisition, the scan size range was fixed to 2 μm with an aspect ratio 3:1. For this experiment 117 images were collected, the first image of the $SrVO_3$ surface in water was obtained after 2 minutes 20 seconds and the last image after 124 minutes and 11 seconds. The scanning frequency was set to 2 Hz, with 256 samples per line for images n°1 to n°78, allowing an acquisition time of 50 seconds, and with 512 samples per line for images n°79 to n°117 for a resulting acquisition time of approximatively 100 seconds. Images were analyzed with the Nanoscope Analysis 1.8 software (Bruker) and gathered in Windows Movie Maker v2.6 to make a movie of the SVO dissolution in water (see the supporting information **S1**). We used one-in-two images for images n°1 to n°78 and all images from n°79 to n°117 to reach a similar interval of time for the video.

Regular X-ray Photoelectron Spectroscopy (XPS) measurements were carried out using a Thermofisher Scientific ESCALab 250 Xi spectrometer with a monochromatic Al-Kα X-ray source (hν = 1486.6 eV). The detection was performed perpendicular to the sample surface using a constant analyzer energy (CAE) mode (pass energy 20 eV), and spectra were recorded with a 0.1 eV energy step. The survey spectrum in **figure 3b** was collected with a pass energy of 100 eV and an energy step of 1 eV. The use of a low-energy electron and ion flood gun was necessary to perform the analysis. Quantification was performed on the C1s, O1s, Sr3d, $V2p_{3/2}$ peak areas after a Shirley type background subtraction using the Thermofisher Scientific Avantage© software. XPS Imaging of the reported STO layers on top of Si substrate was performed in parallel imaging acquisition mode using a 900 μm spot, i.e. photoelectrons from the whole of the field of view (1 mm) are detected simultaneously. Electrons of a given kinetic energy are focused on the channel plate detector to produce a direct image of the sample without scanning. Integrating images from consecutive energies, an average spectrum of the selected area

can be generated. Maps were recorded in the energy range of O1s, Sr3d and V2p, using a 20 eV pass energy and 0.1 eV energy step between each acquisition. XPS imaging of the SVO-STO stack was recorded with a Thermofisher Scientific Nexsa spectrometer with a monochromatic Al-Kα X-ray source (hν = 1486.6 eV) in the "SnapMap" mode. In such imaging mode, the micro-focused beam was rastered across the sample by rapid stage movements, yielding an elementary map (O1s, Sr3d, Ti2p and V2p) with a field of view of 3 mm². Full spectra were acquired at each pixel with pass energy of 150 eV.

The crystal structure of the STO layers were characterized by X-ray diffraction (XRD) analyses using a Bruker D8 Discover diffractometer equipped with a Cu Kα1 radiation source (λ = 0.15406 nm).

ASSOCIATED CONTENT

Supporting Information

The following files are available free of charge on the ACS Publications website at DOI: 10.1021/acs.nanolett….

S1: Video of *in situ* AFM (in liquid-mode) of the SVO thin film dissolution in water with surface nanostructured (MPEG) and associated roughness (root mean square or RMS) evolution in time.

S2: Optical micrographs, AFM analysis and XPS mapping on STO thin-film partially transferred onto Si substrate using PDMS support.

S3: XPS chemical composition tables and associated spectra related to figure 2b.

S4: XPS chemical composition tables and associated spectra related to figure 4c.

S5: Optical micrographs of a 20 nm-thick and 3.9×3.9 mm² square-shaped STO thin film transferred onto Si substrate.

S6: AFM analyses of the STO transferred layer related to figure S5.

S7: XRD analyses of the STO transferred layer related to figure S5.

AUTHOR INFORMATION

Corresponding Author

*E-mail: yoan.bourlier@uvsq.fr.

Author Contributions

The manuscript was written through contributions of all authors. All authors have given approval to the final version of the manuscript.

Notes

The authors declare no competing financial interest.

ACKNOWLEDGMENT

The authors acknowledge the LabEx CHARMMMAT (ANR-11-LABEX-0039) for financial supports, and the French Agence Nationale de la Recherche (ANR) (ANR-17-CE08-0012) in the framework of the POLYNASH project. The authors thank Dr. O. Popova for the preparation of the PLD $SrVO_3$ (SVO) and $SrTiO_3$ (STO) targets. The authors are also grateful to Pr. M. Benore from Michigan University who proofread the manuscript.

ABBREVIATIONS

SL, Sacrificial Layer; SVO, $SrVO_3$; STO, $SrTiO_3$; PDMS, Poly-Di-Methyl-Siloxane; SP, Screen Protector; XPS, X-ray Photoelectron Spectroscopy; AFM, Atomic Force Microscopy; XRD, X-ray Diffraction; SI, Supporting Information.

REFERENCES

(1) Mannhart, J.; Schlom, D. G. *Science* **2010**, 327, 1607−1611.

(2) Rogers, J. A.; Lagally, M. G.; Nuzzo, R. G. *Nature* **2011**, 477, 45−53.

(3) Hwang, H. Y.; Y. Iwasa, Y; M. Kawasaki, M.; B. Keimer, B.; N. Nagaosa, N.; Tokura, Y. *Nat. Mater.* **2012**, 11, 103−113.

(4) Caviglia, A. D.; Gariglio, S.; Reyren, N.; Jaccard, D.; Schneider, T.; Gabay, M.; Thiel, S.; Hammerl, G.; Mannhart, J.; Triscone, J. M. *Nature* **2008**, 456, 624−627.

(5) Park, J. W.; Bogorin, D. F.; Cen, C.; Felker, D. A.; Zhang, Y.; Nelson, C. T.; Bark, C. W.; Folkman, C. M.; Pan, X. Q.; Rzchowski, M. S.; Levy, J.; Eom C. B. *Nat. Commun.* **2010**, 94, 1.

(6) Bark, C. W.; Sharma, P.; Wang, Y.; Baek, S. H.; Lee, S.; Ryu, S.; Folkman, C. M.; Paudel, T. R.; Kumar, A.; Kalinin, S. V.; Sokolov, A.; Tsymbal, E. Y.; Rzchowski, M. S.; Gruverman, A.; Eom, C. B. *Nano Lett.* **2012**, 12, 1765−1771.

(7) Sharma, P.; Ryu, S.; Burton, J. D.; Paudel, T. R.; Bark, C. W.; Huang Ariando, Z.; Tsymbal, E. Y.; Catalan, G.; Eom, C. B.; Gruverman, A. *Nano Lett.* **2015**, 15, 3547−3551.

(8) Huang, M.; Jnawali, G.; Hsu, J.-F.; Dhingra, S.; Lee, H.; Ryu, S.; Bi, F.; Ghahari, F.; Ravichandran, J.; Chen, L.; Kim, P.; Eom, C.-B.; D'Urso, B.; Irvin, P.; Levy, J. *APL Mater.* **2015**, 3, 062502.

(9) Dai, W.; Adhikari, S.; Garcia-Castro, A. C.; Romero, A. H.; Lee, H.; Lee, J.-W.; Ryu, S.; Eom, C.-B.; Cen, C. *Nano Lett.* **2016**, 16, 2739−2743.

(10) Ridier, K.; Aureau, D.; Bérini, B.; Dumont, Y.; Keller, N.; Vigneron, J.; Etcheberry, A.; Domengès, B.; Fouchet, A. *Phys. Rev. B* **2018**, 97, 035146.

(11) Chen, Y.; Casals, B.; Herranz, G. *ACS Appl. Electron. Mater.* **2019**, 1, 810-816.

(12) Hurand, S.; Jouan, A.; Lesne, E.; Singh, G. ; Feuillet-Palma, C.; Bibes, M.; Barthélémy, A.; Lesueur, J.; Bergeal, N. *Phys. Rev. B* **2019**, 99, 104515.

(13) McKee, R. A.; Walker, F. J.; Chisholm, M. F. *Phys. Rev. Lett.* **1998**, 81, 3014–3017.

(14) McKee, R. A.; Walker, F. J.; Chisholm, M. F. *Science* **2001**, 293, 468–471.

(15) Wang, Y.; Ganpule, C.; Liu, B. T.; Li, H.; Mori, K.; Hill, B.; Wuttig, M.; Ramesha R.; Finder, J.; Yu, Z.; Droopad, R.; Eisenbeiser K. *Appl. Phys. Lett.* **2002**, 80, 97−99.

(16) Wei, Y.; Hu, X.; Liang, Y.; Jordan, D. C.; Craigo, B.; Droopad, R.; Yu, Z.; Demkov, A.; Edwards Jr., J. L.; Ooms, W. J. *J. Vac. Sci. Technol. B* **2002**, 20, 1402−1405.

(17) Droopad, R.; Yu, Z.; Li, H.; Liang, Y.; Overgaard, C.; Demkov, A.; Zhang, X.; Moore, K.; Eisenbeiser, K.; Hu, M.; Curless, J.; Finder, J. *J. Cryst. Growth* **2003**, 251, 638–644.

(18) Largeau, L.; Patriarche, G.; Saint-Girons, G.; Delhaye, G.; Hollinger, G. *Appl. Phys. Lett.* **2008**, 92, 031904.

(19) Warusawithana, M. P.; Cen, C.; Sleasman, C. R.; Woicik, J. C.; Li, Y.; Kourkoutis, L. F.; Klug, J. A.; Li, H.; Ryan, P.; Wang, L.-P.; Bedzyk, M.; Muller, D. A.; Chen, L.-Q.; Levy, J.; Schlom D. G. *Science* **2009**, 324, 367–370.

(20) Baek, S. H.; Park, J. Kim, D. M.; Aksyuk, V. A.; Das, R. R.; Bu, S. D.; Felker, D. A.; Lettieri, J.; Vaithyanathan, V.; Bharadwaja, S. S. N.; Bassiri-Gharb, N.; Chen, Y. B.; Sun, H. P.; Folkman, C. M.; Jang, H. W.; Kreft, D. J.; Streiffer, S. K.; Ramesh, R.; Pan, X. Q.; Trolier-McKinstry, S.; Schlom, D. G.; Rzchowski, M. S.; Blick, R. H.; Eom C. B. *Science* **2011**, 334, 958–961.

(21) Hsu, M.-H. M.; Marinelli, A.; Merckling, C.; Pantouvaki, M.; Van Campenhout, J.; Absil, P.; Van Thourhout, D. *Opt. Mater. Express* **2017**, 7, 2030−2039.

(22) Lapano, J.; Brahlek, M.; Zhang, L.; Roth J.; Pogrebnyakov, A.; Engel-Herbert, R. *Nat. Commun.* **2019**, 10, 2464.

(23) Wu, H. W.; Aoki, T.; Posadas, A. B.; Demkov, A.; Smith, D. J. *Appl. Phys. Lett.* **2016**, 108, 091605.

(24) Diaz-Fernandez, D.; Spreitzer, M.; Parkelj, T.; Suvorov, D. *Appl. Surf. Sci.* **2018**, 455, 227–235.

(25) Kikuta, K.; Noda, K.; Okumura, S.; Yamaguchi, T.; Hirano, S. *J. Sol-Gel Sci. Technol.* **2007**, 42, 381–387.

(26) Shibata, T.; Fukuda, K.; Ebina, Y.; Kogure, T.; Sasaki, T. *Adv. Mater.* **2008**, 20, 231−235.

(27) Shibata, T.; Ohnishi, T.; Sakaguchi, I.; Osada, M.; Takada, K.; Kogure, T.; Sasaki T.; *J. Phys. Chem. C* **2009,** *113*, 19096–19101.

(28) Nijland, M.; Kumar, S.; Lubbers, R.; Blank, D. H. A.; Rijnders, G.; Koster, G.; ten Elshof, J. E. *Appl. Mater. Interfaces* **2014**, 6, 2777−2785.

(29) Nijland, M.; Thomas, S.; Smithers, M. A.; Banerjee, N.; Blank, D. H. A.; Rijnders, G., Xia, J.; Koster, G.; ten Elshof, J. E. *Adv. Funct. Mater.* **2015**, *25*, 5140–5148.

(30) Yuan, H.; Nguyen, M.; Hammer, T.; Koster, G.; Rijnders, G.; ten Elshof, J. E. *Appl. Mater. Interfaces* **2015**, 7, 27473−27478.

(31) Matsuba, K.; Wang, C.; Saruwatari, K.; Uesusuki, Y.; Akatsuka, K.; Osada, M.; Ebina, Y.; Ma, R.; Sasaki, T. *Sci. Adv.* **2017**, 3, e1700414.

(32) Boileau, A.; Dallocchio, M.; Baudouin, F; David, A.; Lüders, U.; Mercey, B.; Pautrat, A.; Demange, V.; Guilloux-Viry, M.; Prellier, W.; Fouchet, A.; *ACS Appl. Mater. Interfaces* **2019**, 11, 37302-37312.

(33) Baudouin, F.; Demange, V.; Ollivier, S.; Rault, L.; Brito, A. S.; Maia, A. S.; Gouttefangeas, F.; Bouquet, V.; Députier, S.; Bérini, B.; Fouchet, A.; Guilloux-Viry M. *Thin Solid Films* **2019**, 137682.

(34) Lee, S. A.; Hwang, J.-Y.; Kim, E. S.; Kim, S. W.; Choi, W. S. *Appl. Mater. Interfaces* **2017**, 9, 3246−3250.

(35) Catlin, A.; Walker, W. P.; *J. Appl. Phys.* **1960**, 31, 2135–2139.

(36) Wang, L.; Meric, I.; Huang, P. Y.; Gao, Q.; Gao, Y.; Tran, H.; Taniguchi, T.; Watanabe, K.; Campos, L. M.; Muller, D. A.; Guo, J.; Kim, P.; Hone, J.; Shepard, K. L.; Dean, C. R. *Science* **2013**, 342, 614.

(37) Tien, D. H.; Park, J.-Y.; Kim, K. B.; Lee, N.; Choi, T.; Kim, P.; Taniguchi, T.; Watanabe, K.; Seo, Y. *ACS Appl. Mater. Interfaces* **2016**, 8, 3072-3078.

(38) Li, X.; Zhu, Y.; Cai, W.; Borysiak, M.; Han, B.; Chen, D.; Piner, R. D.; Colombo, L.; Ruoff, R. S. *Nano Lett.* **2009**, 9, 4359–4363.

(39) Kim, K. S.; Zhao, Y.; Jang, H.; Lee, S. Y.; Kim, J. M.; Kim, K. S, Ahn, J.-H.; Kim, P.; Choi, J.-Y.; Hong, B. H. *Nature* **2009**, 457, 706–710.

(40) Lee, Y.; Bae, S.; Jang, H.; Jang, S.; Zhu, S.; Sim, S. H.; Song, Y. I.; Hong, B. H.; Ahn, J.-H. *Nano Lett.* **2010**,10, 490–493.

(41) Suk, J. W.; Kitt, A.; Magnuson, C. W.; Hao, Y.; Ahmed, S.; An, J.; Swan, K.; Goldberg, B. B.; Ruoff, R. S. *ACS Nano* **2011**, 5, 6916–6924.

(42) Chen, X.-D.; Liu, Z.-B.; Zheng, C.-Y.; Xing, F.; Yan, X.-Q.; Chen, Y.; Tian, J.-G. *Carbon* **2013**, 56, 271–278.

(43) Ngoc, H. V.; Qian, Y.; Han, S. K.; Kang, D. J. *Sci. Reports* **2016**, 6, 33096.

(44) Paskiewicz, D. M.; Sichel-Tissot, R.; Karapetrova, E.; Stan, L.; Fong, D. D. *Nano Lett.* **2016**, 16, 534−542.

(45) Bakaul, S. R.; Serrao, C. R.; Lee, M.; Yeung, C. W.; Sarker, A.; Hsu, S.-L.; Yadav, A. K.; Dedon, L.; You, L.; Khan, A. I. *Nat. Comm.* **2016**, 7, 10547.

(46) Lu, D.; Baek, D. J.; Hong, S. S.; Kourkoutis, L. F.; Hikita, Y.; Hwang, H. Y. *Nat. Mater.* **2016**, 15, 1255–1260.

(47) Ji, D.; Cai, S.; Paudel, T. R.; Sun, H.; Zhang, C.; Han, L.; Wei, Y.; Zang, Y.; Gu, M.; Zhang, Y.; Gao, W.; Huyan, H.; Guo, W.; Wu, D.; Gu, Z.; Tsymbal, E. Y.; Wang, P.; Nie, Y.; Pan, X. *Nature Lett.* **2019**, 570, 87−90.

(48) Baek, D. J.; Lu, D.; Hikita, Y.; Hwang, H. Y.; Kourkoutis, L. F. *Appl. Mater. Interfaces* **2017**, 9, 54–59.

(49) Zhu, Y.; Dai, Y.; Lai, K.; Li, Z.; Huang, B. *J. Phys. Chem. C* **2013**, 117, 5593−5598.

(50) Boileau, A.; Cheikh, A.; Fouchet, A.; David, A.; Escobar-Galindo, R.; Labbé, C.; Marie, P.; Gourbilleau, F.; Lüders, U. *Appl. Phys. Lett.* **2018**, 112, 021905.

(51) Mirjolet, M.; Vasili, H. B.; López-Conesa, L.; Estradé, S.; Peiró, F.; Santiso, J.; Sánchez, F.; Machado, P.; Gargiani, P.; Valvidares, M.; Fontcuberta J. *Adv. Funct. Mater.* **2019**, 29, 1904238.

(52) Boileau, A.; Cheikh, A.; Fouchet, A.; David, A.; Labbé, C.; Marie, P.; Gourbilleau, F.; Lüders, U. *Adv. Opt. Mater.* **2019**, *1801516*.

(53) Bérini, B.; Demange, V.; Bouttemy, M.; Popova, E.; Keller, N.; Dumont, Y.; Fouchet, A. *Adv. Mater. Interfaces* **2016**, *3*, 1600274.

(54) Coq-Germanicus, R.; Bourlier, Y.; Euchin, M.; Bérini, B.; Dumont, Y.; Aureau, D.; Fregnaux, M.; Biadala, L.; Berthe, M.; Notot, V.; Luders, U.; David, A.; Prellier, W.; Fouchet, A. *submitted*.

(55) Bourlier, Y.; Frégnaux, M.; Bérini, B.; Fouchet, A.; Dumont, Y.; Aureau, D. *ChemNanoMat* **2019**, 5, 674−681.

(56) Ohnishi, T.; Shibuya, K.; Lippmaa, M.; Kobayashi, D.; Kumigashira, H.; Oshima, M.; Koinuma, H. *Appl. Phys. Lett.* **2004**, 85, 272.

(57) Bachelet, R.; Sánchez, F.; Palomares, F. J.; Ocal, C.; Fontcuberta, J. *Appl. Phys. Lett.* **2009**, 95, 141915.

(58) Connell, J. G.; Isaac, B. J.; Ekanayake, G. B.; Strachan, D. R.; Seo S. S. A. *Appl. Phys. Lett.* **2012**, 101,251607.

(59) Bérini, B.; Fouchet, A.; Popova, E.; Tessier, M.; Denise, S.; Dumont, Y.; Keller, N. *Appl. Phys. A* **2010**, 101, 47–51.

(60) *Supporting information of* Chen, X.-D.; Liu, Z.-B.; Zheng, C.-Y.; Xing, F.; Yan, X.-Q.; Chen, Y.; Tian, J.-G. *Carbon* **2013**, 56, 271–278.

(61) Mirjolet, M.; Sánchez, F.; Fontcuberta, J. *Adv. Funct. Mater.* **2019**, 29, 1808432.

FIGURES

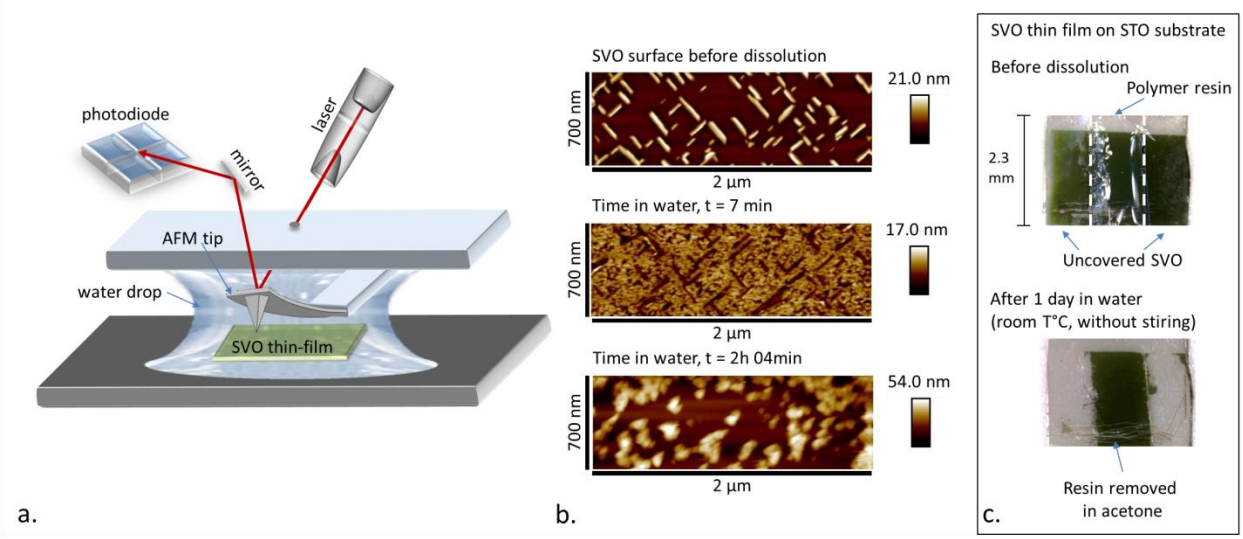

Figure 1: Dissolution of the entire SVO layer with water, (a) Outline of the AFM analysis used in liquid mode for *in situ* observation; **(b)** Three AFM *in situ* images taken at different times, related to the video of the SVO dissolution (see supporting file); and **(c)** Observation of the SVO smooth thin film dissolution using a polymer resin mask. After 1 day in water, the uncovered zones are removed. Both SVO nanostructured and smooth samples are 40 nm-thick.

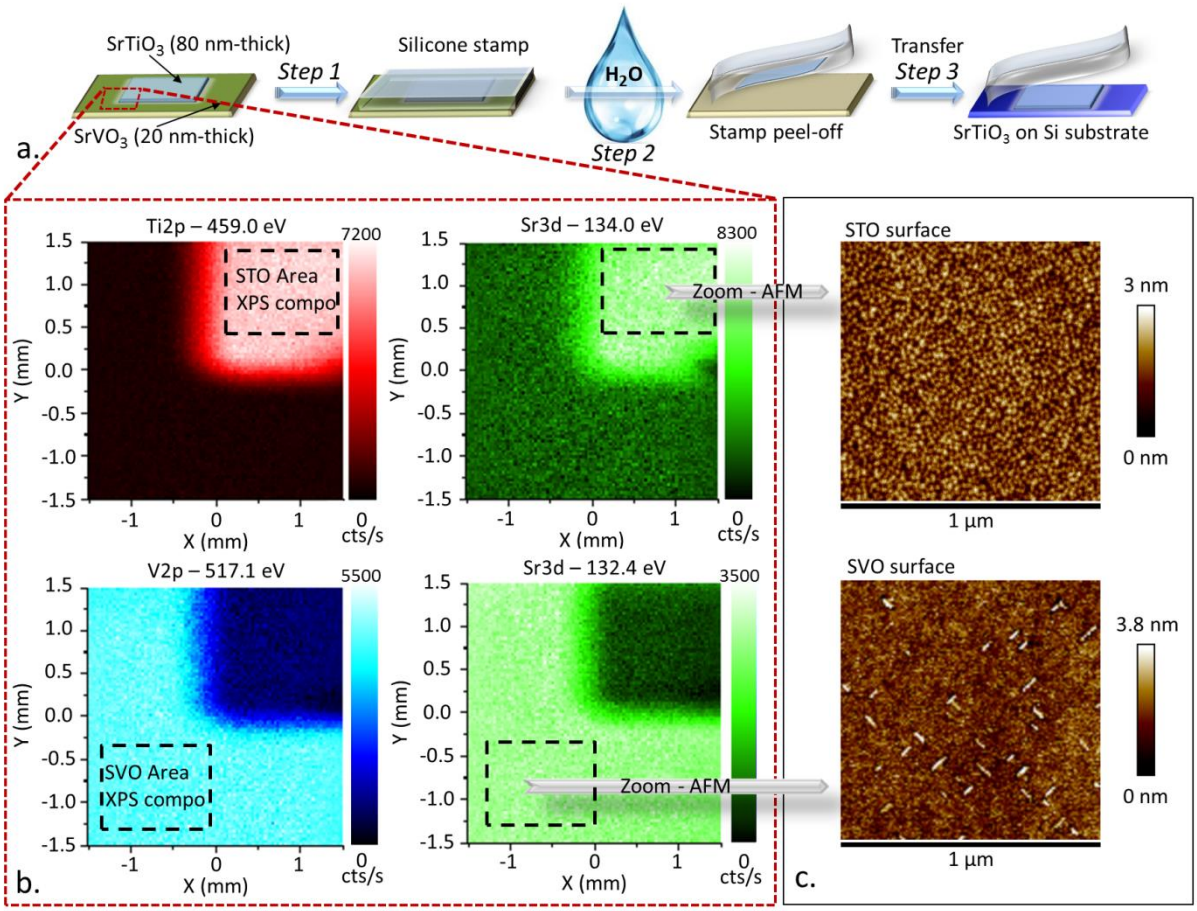

Figure 2: SVO used as a sacrificial layer for perovskite thin film transfer onto Si substrate, (a) Layout of the transfer process using a STO/SVO stack deposited by PLD onto $SrTiO_3$ (100) substrate and PDMS film used as stamp and intermediate support for transferring STO thin film onto Si substrate after dissolving the SVO layer under water; **(b)** XPS mapping analysis of the STO and SVO focused areas of the sample before processing the transfer, and **(c)** corresponding AFM analysis of the STO and SVO focused areas.

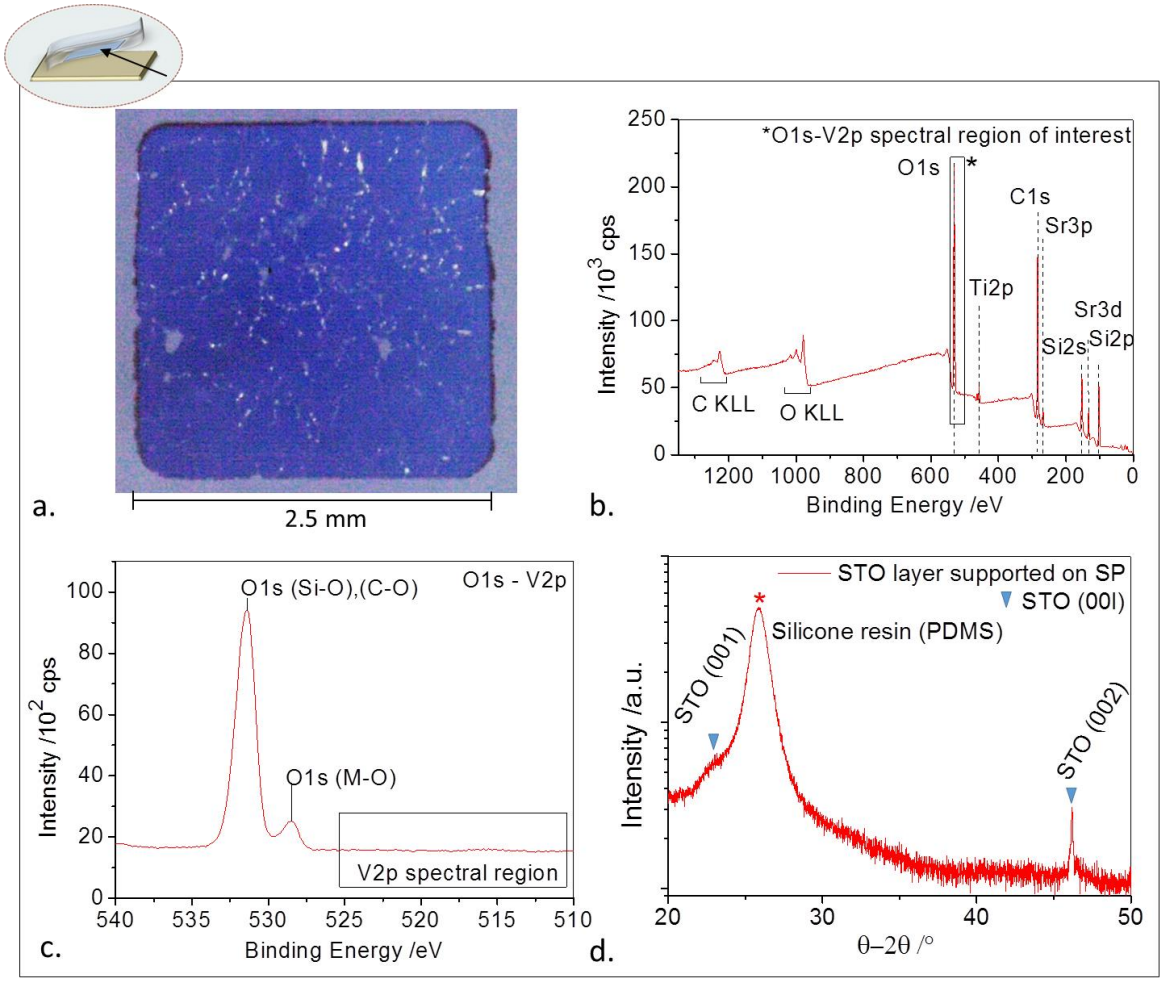

Figure 3: Analysis of the STO layer supported by the SP film, (a) photography of the freestanding STO thin film on SP film, **(b)** XPS survey of the reverse side of the STO thin film; **(c)** High resolution spectra of the O1s-V2p region of interest with no vanadium detected; **(d)** X-ray Cu $K\alpha_1$ diffractogram of the SP supported STO transferred layer with STO (001) and (002) Bragg peaks.

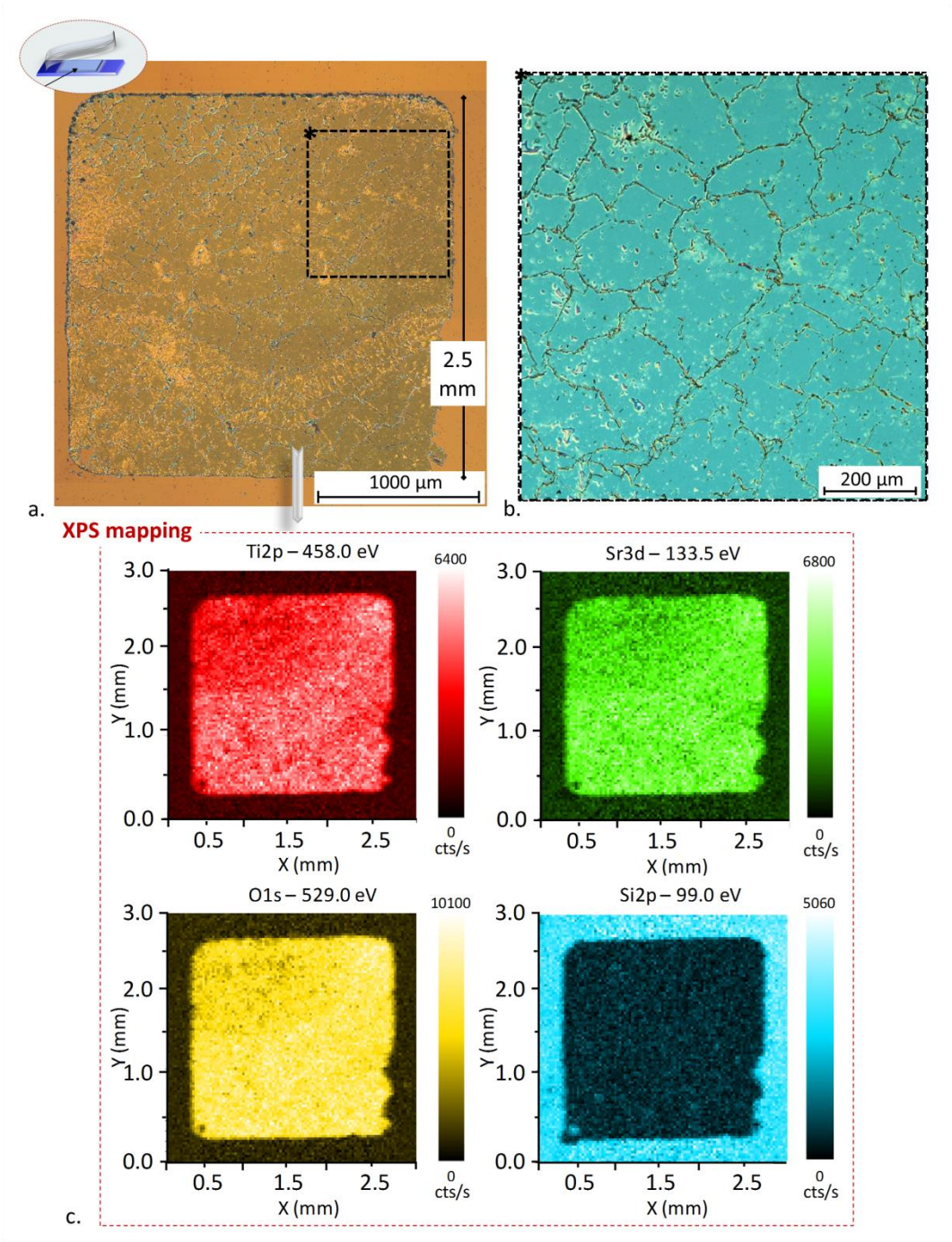

Figure 4: STO thin film transferred onto Si substrate, (a) optical micrograph reconstruction of the STO transferred layer, **(b)** micrograph of a particular zone of interest, and **(c)** XPS mapping of the related zone of interest showing Ti2p, Sr3d, O1s, and Si2p spectral signatures.

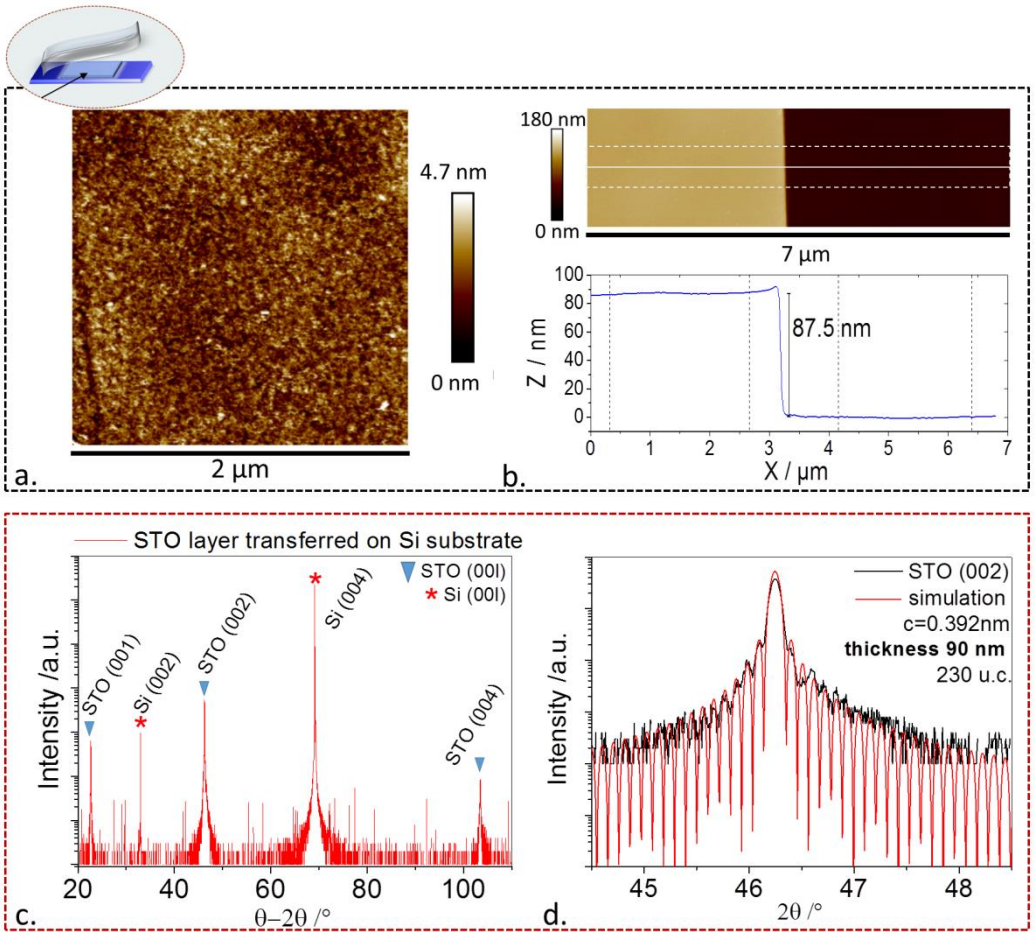

Figure 5: STO transferred layer onto Si substrate with physical properties conserved, (a) AFM roughness analysis, **(b)** AFM thickness measurement, **(c)** X-ray Cu $K\alpha_1$ diffractogram of the STO transferred layer, with (00l) crystal orientation revealed, and **(d)** high resolution X-ray diffraction near the STO (002) Bragg peak with Laue oscillations.